PAPER

Check for updates

Fe–Ni porphyrin/mesoporous titania thin film electrodes: a bioinspired nanoarchitecture for photoelectrocatalysis†

Facundo C. Herrera, [ID] [ab] Rolando M. Caraballo, [ID] [c] Priscila Vensaus, [ID] [a] Galo J. A. A. Soler Illia [ID] [a] and Mariana Hamer [ID] *[d]

Porphyrin and porphyrinoid derivatives have been extensively studied in the assembly of catalysts and sensors, seeking biomimetic and bioinspired activity. In particular, Fe and Ni porphyrins can be used for the hydrogen evolution reaction (HER) and oxygen evolution reaction (OER) by immobilization of these molecular catalysts on semiconductor materials. In this study, we designed a hybrid material containing a crystalline mesoporous TiO_2 thin film in which the catalytic centres are Ni-porphyrin (NiP), Fe-porphyrin (FeP), and a NiP/FeP bimetallic system to assess whether the coexistence of both metalloporphyrins improves the OER activity. The obtained photoelectrodes were physicochemically and morphologically characterized through high-resolution FE-SEM images, UV-vis and Raman spectroscopies, cyclic voltammetry, and impedance measurements. The results show a differential behavior of the mono- and bimetallic porphyrin systems, where the Fe(III) centre in FeP may increase the acidity and lower the reduction potential of the $Ni^{2+/3+}$ couple when co-deposited with NiP leading to an improved photoelectrochemical water-oxidation performance. We have validated the cooperative effect of both metal complexes within this novel system, where the μ-peroxo-bridged interaction between Fe and Ni is integrated into a supramolecular heterometallic structure of porphyrins.

Introduction

Biomimicry involves taking advantage of strategies observed in nature to address challenges in human design, making use of the sophisticated structures developed by organisms, shaped through eons of survival and natural selection as the most competitive.[1] By closely observing and emulating nature's optimal shapes and ecosystems, the refined knowledge derived from these processes can serve as inspiration for the intelligent design of more efficient materials.

Porphyrins and metalloporphyrins are macrocyclic molecules that play key roles in nature, such as antennae for light energy harvesting and as the reaction centre of many enzymes in biological systems. In the case of metalloporphyrins, reduction, and oxidation reactions are catalyzed through different mechanisms, generally ruled by the metal centre and the axial ligands coordinated to it. Some enzymes contain porphyrin bimetallic systems as the catalytic centre, in which the existence of a metal–metal interaction plays a major role in the enzymatic activity.[2,3] For example, the soluble di-iron methane mono-oxygenase (sMMO) presents a Fe–Fe interaction, and the di-copper tyrosinase has a Cu–Cu interaction. Heterobimetallic centres also participate as catalysts, such as the Ni–Fe couple for the conversion of protons into hydrogen in hydrogenases, and the Fe–Cu in cytochrome c oxidases that promote the efficient reduction of O_2 to H_2O, among others.[4–6] Therefore, porphyrin and porphyrinoid derivatives have been extensively studied for applications in reaction catalysis with a biomimetic approach. These include bimetallic interactions, where the combination of two metalloporphyrins has a synergistic effect.[5–7]

Furthermore, porphyrins can be immobilized on solid supports, such as zeolites or metal oxides. The combination of porphyrins and materials with an organized structure further extends the possibilities for application. In these hybrid materials, porphyrins have different functions, such as the reaction centre in heterogeneous catalysts or as sensitizers in photochemical reactions, where they absorb light and transfer this energy to a co-catalyst, like a metal oxide, to drive a chemical reaction. In systems with metalloporphyrins, the metal ion, typically iron, manganese, nickel, copper, or cobalt, acts as the reaction centre, while the solid support provides a high surface

a Instituto de Nanosistemas, Escuela de Bio y Nanotecnología, Universidad Nacional de General San Martín (INS-UNSAM)-CONICET, 1650, San Martín, Argentina

b Laboratorio Argentino Haces de Neutrones-CNEA, Av. Gral. Paz 1499, Villa Maipú, Argentina

c INEDES, UNLu-CONICET, Av. Constitución y Ruta Nac. No. 5 (CP6700), Luján, Argentina

d Instituto de Ciencias, Universidad Nacional de General Sarmiento-CONICET, Juan María Gutiérrez 1150 (CP1613), Los Polvorines, Argentina. E-mail: mhamer@campus.ungs.edu.ar

area for the catalyst and helps to stabilize the reaction intermediates. For example, Fe and Ni porphyrins have been used for hydrogen and oxygen evolution reactions through the immobilization of these molecular catalysts onto photoelectrode materials.[8–11] Also, Ni- and Co-porphyrin multilayers on reduced graphene oxide (rGO) sheets, where stacking interactions with porphyrins provide electric properties, are reported as a novel bifunctional catalyst for oxygen evolution reaction (OER) and oxygen reduction reaction (ORR).[12] Recently, it has been demonstrated that the combination of Ni and Fe in a bimetal-based system can enhance OER activity noticeably.[13,14] Polymeric carbon nitride with dispersed N-coordinated Ni–Fe sites was used for the OER process showing that the Ni–Fe co-doped film had higher electrocatalytic activity than monometallic-doped catalysts in 1 M KOH, demonstrating that Ni–Fe dual-metal sites significantly favor the OER process.[13] A similar behavior was observed in a Ni–Fe bimetallic MOF/graphene oxide composite, where the optimized material exhibited higher OER catalytic performance as well as stability in an alkaline solution.[11]

TiO$_2$ has served as the standard material for photocatalytic processes, being the most studied material with a wide band gap of 3.2 eV that requires UV irradiation for photocatalytic activation. However, the challenge nowadays is promoting visible light-active photocatalysts.[1] Following this approach, in our previous work, we described new hybrid materials based on a mesoporous TiO$_2$ thin film doped with Prussian blue analogs, Zn-porphyrin, or carbon dots with great potential in photoelectric applications.[15–17] Here we evaluate whether the coexistence of Fe and Ni metalloporphyrins can give a relevant OER activity as molecular catalysts while immobilized in a crystalline mesoporous titania thin film (cMTTF). These films constitute a photoactive, robust, reproducible, and high-surface-area platform for porphyrin immobilization.[18] For this purpose, we have designed a new porphyrin hybrid material by impregnation deposition of a Ni-porphyrin (NiP) and a Fe-porphyrin (FeP) to form a bimetallic NiP/FeP system on a cMTTF. The samples are named f-NiP, f-FeP, and f-NiP/FeP when referring to the functionalized cMTTF, to distinguish them from the porphyrins in solution. We have thoroughly characterized this system and analyzed the cooperative effect of both metal complexes, which resulted in a heightened catalytic activity for the bimetallic surface.

Experimental

Materials and reagents

Fe(III) and Ni(II) 5,10,15,20-[meso-tetrakis(N-methylpyridyl)porphine] (FeP and NiP, respectively) were purchased from Frontier Scientific. TiCl$_4$, non-ionic block-copolymer Pluronics F127, and absolute ethanol were obtained from Merck. Fluorine-doped tin oxide (FTO) substrates were purchased from Delta Technologies. Other necessary reagents were acquired from Sigma-Aldrich. All chemicals were reagent grade and were used without further purification. Water was deionized and filtered using a Millipore water purification system (18 MΩ).

Crystalline mesoporous TiO$_2$ thin films

Crystalline mesoporous titania thin films (cMTTF) were obtained according to literature procedures.[19] Initial sols were obtained by mixing TiCl$_4$, ethanol, non-ionic block-copolymer template Pluronics F127, and water in a $1 : 40 : 5 \times 10^{-3} : 10$ molar ratio. Films were deposited by dip-coating on FTO-covered glass substrates. First, a dense TiO$_2$ layer was deposited at 35 °C, 20% relative humidity (RH), and 1 mm s^{-1} withdrawal rate. This layer was stabilized at 200 °C for 30 min. Subsequently, the mesoporous TiO$_2$ layer was deposited at 35 °C, 35% RH, and 2 mm s^{-1} withdrawal rate. As-prepared films were aged 30 min at 50% RH. A further thermal treatment was carried out by heating 30 min at 60 °C, 30 min at 130 °C, and 2 h at 350 °C, with a heating ramp of 1 °C min^{-1}. This technique gives a crack-free MTTF, with a highly organized array of pores on a grid-like structure. Films with 40% pore volume and 180 nm thickness were used in this work. Considering the thickness of the mesoporous film, there are 4.57×10^{-5} g of TiO$_2$ per cm^2.

Metalloporphyrin functionalized crystalline mesoporous TiO$_2$ thin films (f-MP)

The modification of the cMTTF with MP (FeP, NiP, or NiP/FeP) was performed as in our previous reports,[16,20] by 48 h immersion in an MP solution in water, with 30 μM total concentration. After adsorption, f-MP was rinsed with deionized water, air-dried, and placed in a vacuum oven at 60 °C to dry for 6 h. The obtained hybrid materials were f-FeP, f-NiP, and f-NiP/FeP, respectively. The general synthetic method is depicted in Scheme S1.†

Characterization

Field Emission Scanning Electron Microscopy (FE-SEM) images were taken on an SEM Zeiss Supra 40 equipped with a field emission gun from CMA – FCEN-UBA.

Raman measurements were performed using a "Senterra" Raman microscope (Bruker) under a laser excitation of 532 nm (1 mW power). The spectra were collected with a resolution of ~3–5 cm^{-1} and an integration time of 10 s.

UV-vis absorption spectra were recorded with a Shimadzu UV-3600 PLUS UV-vis-NIR spectrometer (185–3300 nm) in forward transmission mode using normal incidence geometry. The photocatalytic measurements were recorded using an Ocean Optics H2 spectrophotometer in the range 220–1100 nm, resolution 0.08–7.12 nm, illuminating with a deuterium and tungsten lamp, in 1 cm path-length quartz cuvette and using MilliQ water as blank. MP load was estimated using the Lambert–Beer law and the molar extinction coefficient of FeP and NiP in solution, as previously reported.[16,21] Absorbance in the modified films UV-vis spectra at 398 nm ($\varepsilon = 1.02 \times 10^5$ M^{-1} cm^{-1}) and 419 nm ($\varepsilon = 1.22 \times 10^5$ M^{-1} cm^{-1}) is due to FeP and NiP, respectively. The cMTTF thickness is $l_{MTTF} = 180$ nm (1.8×10^{-5} cm).

X-ray reflectometry (XRR) measurements were performed with Bruker D8 Eco equipment using an incident beam of Cu Kα

radiation. To obtain accurate density values, measurements were performed under low-humidity conditions. This is a relevant experimental aspect, as the condensation of atmospheric moisture within the pores could lead to a severe underestimation of the film mesoporosity. NiP, FeP, and NiP/FeP loadings were estimated using XRR data following the procedure reported previously.[22] Calculations are described in the ESI.†

X-ray photoelectron spectroscopy (XPS) measurements were performed on a SPECS Flexmod using a monochromatic source with Al anode (1486.61 eV), a power of 100 W, and a potential difference of 10 kV. A charge compensation with low energy electrons (flood gun) was required, finding an optimum flux of 2.0 eV and 30 μA. XPS spectra of the whole sample were measured ("survey"), and higher precision measurements were made in the C 1s, Ni 1s, Ti 2p, Fe 2p, O 1s, and N 1s regions used.

Electrochemical and photoelectrochemical measurements were performed in a custom-made photoelectrochemical cell, with a standard 3-electrode system (WE: f-MP or cMTTF, RE: Ag/AgCl (KCl 3 M), CE: Pt foil). All potentials were converted to RHE. A Metrohm Autolab potentiostat coupled with Nova software was used. Linear sweep voltammetry was carried out at 10 mV s^{-1} with chopped illumination. The main light source was an Abet Technologies Sun 2000 Solar Simulator equipped with a 150 watt xenon short arc lamp and an irradiating power of 1 sun (AM 1.5) was also used. Irradiation was performed perpendicular to the electrode surface, on the f-MP face. Current densities refer to the geometrical area of the submerged samples. All (photo)electrochemical experiments were conducted in 0.1 M phosphate buffer solution at pH 7 at room temperature (~25 °C).

Electrochemical Impedance Spectroscopy (EIS) measurements were performed using the same Metrohm Autolab potentiostat and electrode configuration, in 0.1 M phosphate buffer solution (pH 7). The Nyquist diagrams were recorded in the frequency range between 10 kHz and 0.01 Hz at room temperature.

Results and discussion

Crystalline mesoporous titania thin films (cMTTF) were synthesized as previously reported,[19] and physicochemical and morphologically characterized. The anatase structure provides them with good electrical conductivity, which together with their transparency in the visible spectral range makes them ideal for photoelectrochemical applications. The high surface area with ca. 40% porosity also allows optimal functionalization with molecules. High-resolution FE-SEM images reveal the typical morphology and ordering degree of the pore array of a cMTTF (Fig. S1†).

The performance of NiP and FeP in homogeneous catalysis has been tested as standalone systems or forming bimetallic composites.[9–11] For NiP/FeP combinations, efficiency depends on stoichiometry[23] and it was proved that a 1 : 1 molar ratio is optimal, resulting in the formation of molecular arrays.[7,24] Thus, we studied the cMTTF functionalization with FeP and NiP monometallic systems and compared them to the same

treatment with NiP/FeP heterobimetallic couple in a 1 : 1 ratio. Metalloporphyrin functionalized cMTTF systems (f-FeP, f-NiP, and f-NiP/FeP) were prepared with the same total porphyrin concentration in solution, namely 30 μM.

Raman spectroscopy was used for film characterization since the porphyrins have resonance Raman active modes. Spectral analysis proved to be very useful in determining the vibrational modes of the loaded molecules, providing a structural fingerprint by which we can identify each porphyrin system and the interactions between them.

Fig. 1 shows the Raman spectra for f-FeP, f-NiP, and f-NiP/FeP. Excitation with a 532 nm laser for Raman scattering is resonant with the Q absorption bands of the mono and bimetallic composites.[7,24] Table S1† summarizes the assignments for the full spectrum. Pyridinic and other characteristic porphyrin bands dominate the spectra in all the composites, while weak metal–ligand vibrations are observed.[7] The three spectra are similar but have some specific differences, the main one being the strong increase of intensity for the band at 565 cm^{-1} in the f-NiP/FeP spectrum. This arises from the formation of an O–O in a peroxide state on a Fe–O–O moiety, where the band corresponds to the Fe–O stretch.[25] Furthermore, this band is absent in f-NiP and very weak in f-FeP at 562 cm^{-1}, indicating that the presence of both metalloporphyrins is needed for its clear appearance. This strong signal is characteristic of μ-peroxo bridged dimers.[26] Therefore, we can assign it to a heterobimetallic dimer as the one shown in the inset of Fig. 1. Furthermore, the broadening and intensity increase of the band at 812 cm^{-1} could be assigned to the formation of the Ni^{3+}–O bond.[27] This vibrational mode is shifted to higher energies compared to its analogous Ni^{2+}–O because the O–O negative charge density is delocalized on the porphyrin ring, changing nickel's apparent oxidation state.[27,28]

In order to study the spectrophotometric properties, we performed an analysis of the UV-vis spectra after cMTTF functionalization (Fig. 2), observing band shifts for both monometallic systems. The f-FeP spectrum shows a peak at 428 nm that is red-shifted by 5 nm relative to FeP in solution (423 nm, Fig. S2†).[29] The position of the same band for NiP shifts from
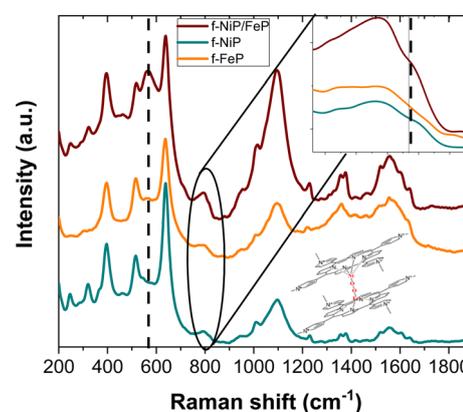

Fig. 1 Raman spectra of f-FeP, f-NiP, and f-NiP/FeP. Excitation wavelength: 532 nm. Inset: Scheme of the μ-peroxo bimetallic dimer between FeP and NiP.
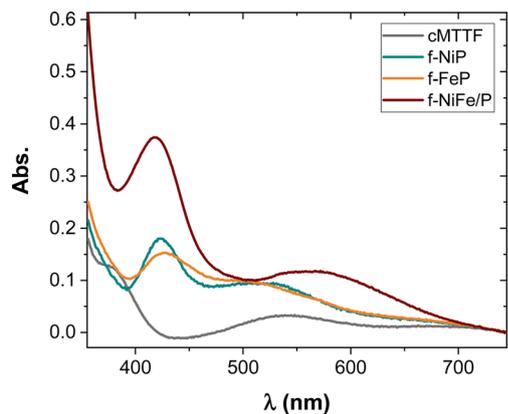
Fig. 2 UV-vis absorption spectra of cMTTF, f-FeP, f-NiP, and f-NiP/FeP after air baseline correction.

419 nm in solution to 423 nm when in f-NiP form, due to axial coordination to the surface.[30] The combination in f-NiP/FeP shows the Soret band at 418 nm, in agreement with the formation of a dimer connecting both metallic centres[7] and with the presence of the Ni^{3+}–O moiety observed in Raman spectra.[27] Also, the intensity of this band nearly doubles that of the monometallic systems, even when the total porphyrin concentration in the synthetic procedure is the same. This increase is assigned to the presence of the dimer, which enables a higher porphyrin loading through the μ-peroxo bridge, together with the formation of a π–π stacked structure of the porphyrin ring (H- or J-aggregates) where the porphyrins align in a parallel fashion and draw near, assuming a more condensed and inflexible conformation.[31–33] The noted phenomenon stems from the overlapping electronic transitions of the two metalloporphyrins. Importantly, this occurrence is unique to the combination of FeP and NiP, resulting in a substantial formation of mixed-valence heteronuclear complexes. Similar results have been reported with diverse ligands, underscoring that the functional behavior is dictated by the orientation of the two metal centers.[7,34–37]

It is worth mentioning that in this case no new absorption bands are observed, nor evidence of pore-clogging or residues generated outside the pores was seen in the FE-SEM images (Fig. S1†), reflecting that in this case MP does not self-assemble or aggregate on the outer surface. The amount of immobilized MP in the modified films was estimated using normalized UV-vis spectra (Fig. S2†) and the XRR patterns data (Fig. S3†). An amount of 11–13 μmol MP per g cMTTF was obtained using the absorbance estimation, which corresponds to ~17 MP molecules per pore. This value is in close agreement with the one calculated using the XRR results (see ESI†).

XPS spectra of the photoelectrodes further revealed the presence of C, N, O, Fe, and Ni elements within the cMTTF. In the Fe 2p XPS spectra (Fig. 3A), two Fe 2p peaks, attributable to Fe $2p^{3/2}$ and Fe $2p^{1/2}$ signals, are found at 710 and 715 eV, respectively, indicating that FeP is present in both photoelectrodes as Fe(III).[10,38] However, in the f-NiP/FeP sample, the peak at 715 eV is shifted to lower binding energies.[10,38] The strong electron-withdrawing environment in this composite

helps explain the positive shift of the putative Fe(III) component of Fe–N–C[38] and a differential catalytic performance in the bimetallic photoelectrode.[10] In addition, only a very weak peak around 854 eV can be observed in the Ni 2p spectra, which can be attributed to Ni $2p^{3/2}$ in the sample f-NiP (Fig. 3B). In the f-NiP compound, only the amount of NiP is high enough to detect Ni $2p^{3/2}$ through XPS analysis in these films. In other words, for the f-NiP sample, nickel porphyrins are present at 100%, and the signal is weak. In contrast, for the f-NiFeP sample, the proportion of porphyrins decreases by half, resulting in a significantly weaker nickel signal that overlaps with the background noise.

In the N 1s spectra, a single band at 399 eV (Fig. S4†) can be ascribed to the four chemically equivalent N atoms which are bound to the central Fe atom in the porphyrin ring which is usually associated in the literature with the catalytic Me–N–C active site. In comparison, the pyridinic nitrogen appears at 398.3 eV and a little peak at around 402 eV can be observed ascribed to the π–π satellite.[38,39] The interaction between NiP and FeP *via* the μ-peroxo bridge can be also elucidated by the spectral deconvolution of N 1s peaks because of their eV value. The shift in the Me–N peak is consistent with the formation of the dimer, acording to the analysis above.[38,40] Additionally, the five peaks observed in the C 1s region of the XPS spectra (Fig. S5†) imply the presence of five different binding energies for carbon. Carbon may be involved in different types of bonds: C–C and C=C (285 eV), C=N (286 eV), π–π* transitions (292 eV and 293), and C–N (295 eV).[40–42] This result depicts that, when NiP and FeP are co-deposited, π–π interactions and the μ-peroxo bridge play a key role in order to obtain the dimer adduct. Furthermore, although in the O 1s XPS spectra (Fig. 3C) typical TiO_2 bands are observed at 530–531 eV, which are related to the oxygen O–Ti–O in the crystal lattice and the Ti–O–H bond respectively,[43] different signals are observed in the nanocomposites spectra. The f-FeP O 1s spectrum shows that oxygen molecules can coordinate to the FeP molecules on the central Fe atoms, most likely in the form of an end-on binding mode, and typical sharp equivalent fitted subpeaks at 531 and 533 eV are observed.[44] While in the f-NiP spectrum sharp fitted subpeaks were observed at a binding energy of approximately 531 and 532 eV that can be attributed to the lattice oxygen of the Ni–O in f-FeP/NiP oxide (532 eV), and oxygen vacancies (Ov, 530.6 eV). This Ov species can be used as electron donors to optimize the electronic structure in the catalyst.[10,45–47]

After the structural analysis, the photoelectrochemical OER performance was analyzed (Fig. 4). As shown in the initial LSV curves in the dark (Fig. 4A), MP-modified films presented anodic peaks related to the porphyrin nature, which are absent in bare cMTTF, and further activity enhancement was obtained in the chronoamperometry at 1.23 V *vs.* RHE (Fig. 4B) with the incorporation of the bimetallic porphyrin system. This was expected since an activation process takes place during water oxidation due to the surface structural changes of Ni–Fe-based catalysts.[48,49] The strong increase in the anodic current above 0.90 V (*vs.* RHE) and beyond the metal oxidation peaks can be assigned to the electrocatalytic oxidation of water to molecular oxygen. It is worth noticing that in the bimetallic
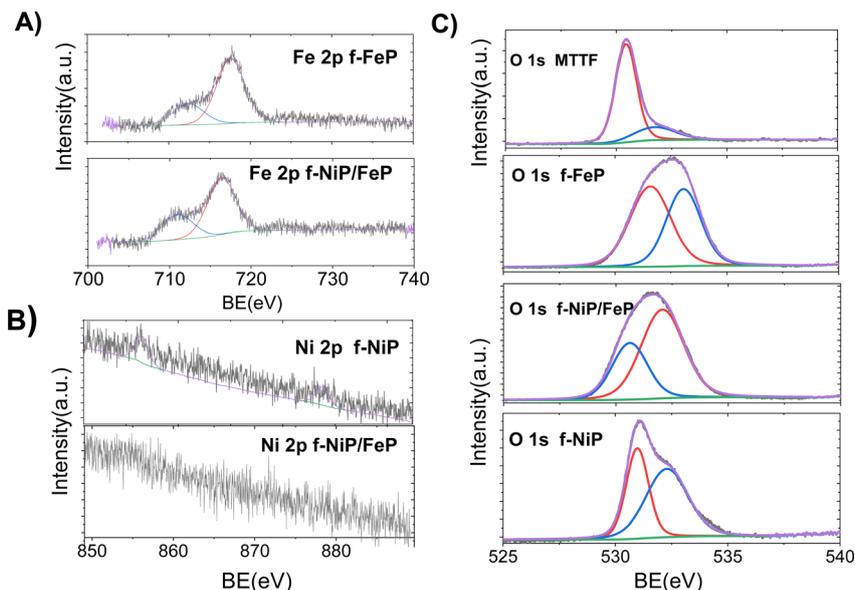
Fig. 3 High-resolution XPS spectra of (A) Fe 2p for f-FeP and f-NiFeP, (B) Ni 2p for f-NiP and f-NiFeP, and (C) O 1s for cMTTF, f-FeP, f-NiP, and f-NiFeP.

photoelectrode nickel oxidation wave was shifted to lower potentials. This is caused by the presence of the NiP/FeP dimer, where the Fe^{3+} centre may increase the acidity of the of OH_x (aqua/hydroxo) moieties that are coordinated to the porphyrin nickel centre, lowering the reduction potential for the $Ni^{3+/2+}$ couple. Consequently, a greater amount of Ni^{3+} in the f-NiP/FeP photoelectrodes is available, promoting an increased oxyl character and leading to a higher OER activity in these films.[48–50] Fig. S6† shows the LSV with and without illumination for each photoelectrode it is worth noticing that the intensity of the LSV anodic currents shifted to lower potentials under illumination, denoting that the incident light promotes the catalytic process. Furthermore, Fig. S6† may indicate that the better performance with the metalloporphyrins is due to the increased absorption and their catalytic effect more than the electrocatalytic effect of cMTTF.

Fig. 4B presents the chronoamperometry measurements at 1.23 V *vs.* RHE for the studied photoelectrodes, where illumination was periodically switched ON:OFF at intervals of 50 seconds with incident light from a solar simulator. A noticeable increase in current is observed in the modified cMTTFs, with the bimetallic functionalization leading to the largest enhancement (237%). The rise in photocurrent observed in f-NiP/FeP can be explained by the presence of NiP/FeP dimers which result in a higher absorbed photon flux and increase the presence of photogenerated charge carriers. Also, the NiP/FeP dimer likely acts as a better OER catalyst, as described above.

The photocurrent values per unit geometrical area were registered in the 40–100 $\mu A\ cm^{-2}$ range at 1.23 V *vs.* RHE, aligning with recent reports on cMTTF.[51,52] These values, which may seem lower than those documented for other TiO_2 materials, arise from the low thickness and thus low amount of
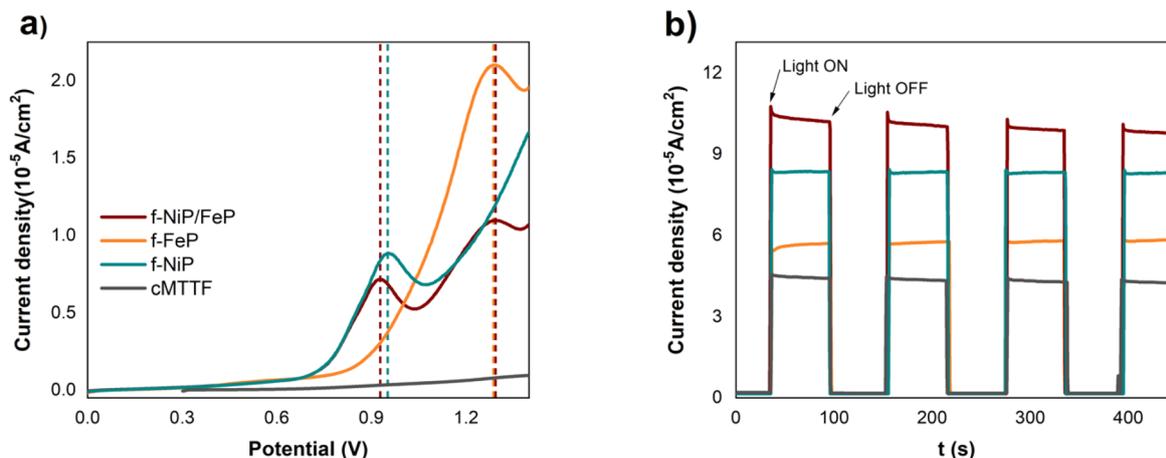

Fig. 4 (a) LSV in the dark and (b) chronoamperometry at 1.23 V *vs.* RHE with chopped solar simulator light, for cMTTF (black), f-FeP (orange), f-NiP (light blue), and f-NiP/FeP (purple).
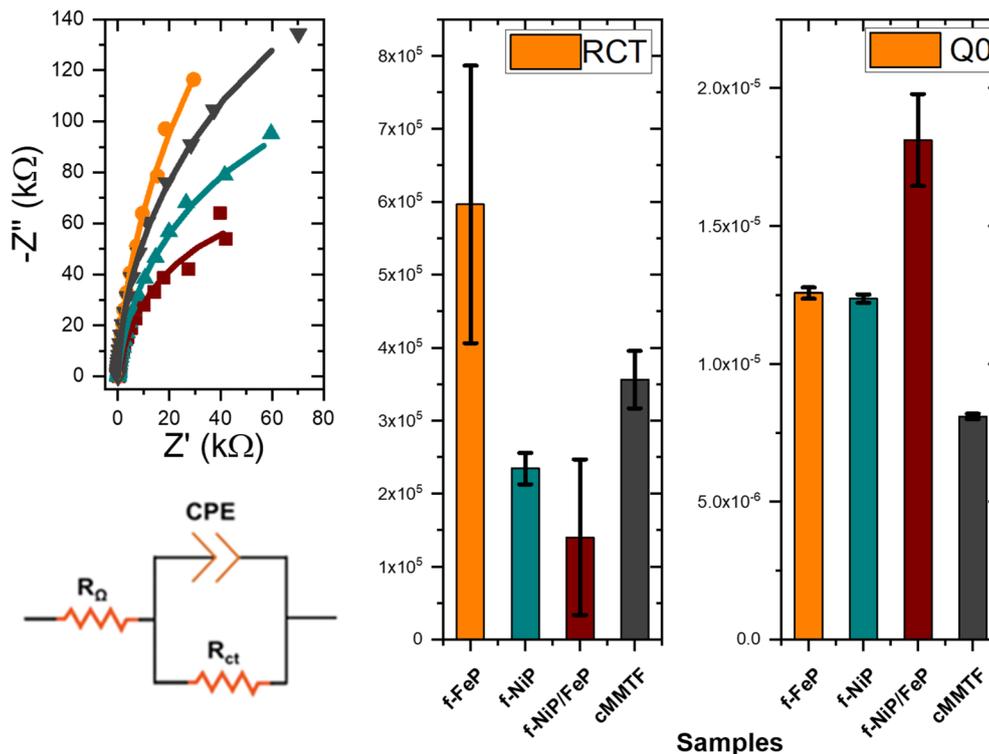
Fig. 5 R_{ct} and Q_0 as obtained by fitting the impedance spectrum for cMTTF, f-FeP, f-NiP, and f-NiP/FeP illumination, at 1.23 V *vs.* RHE.

matter in the samples (approximately 200 nm compared to 1–2 μm in typical reports of nanotubes or P-25 films).[53–55]

Even though LSV at higher potentials is desirable, porphyrins could suffer irreversible oxidation in this region, interfering with our determination. Therefore, higher potentials were avoided.

EIS measurements were performed to investigate the composites' heterogeneous electron transfer rate and photoelectrochemical properties. The occurrence of kinetic and diffusion-controlled processes was determined by modeling the shape of the Nyquist plot of the impedance spectrum of samples measured in the dark and under illumination (Fig. 5 and S7†). The resistance in the high-frequency region, which is related to the solution resistance (R_Ω), resulted in the range of 100–300 Ω for all the films. cMTTF and the modified photoelectrodes exhibit a semicircle associated with the charge transfer resistance (R_{ct}).[56] As expected, these semicircles become smaller under illumination due to the appearance of photogenerated charge carriers. The Nyquist spectra under illumination were fitted with a Randles circuit in the range from 10 kHz to 0.1 Hz (smaller frequencies lead to high noise). The estimated R_{ct} values followed the order cMTTF ∼ f-FeP > f-NiP ∼ f-NiP/FeP (Table S2† and Fig. 5). The lowest R_{ct} value for f-NiP/FeP indicates the highest charge transfer rate and easier formation of active species for OER. This contributes to the highest catalytic activity among the systems under study, considering their similar surface area, and is consistent with the presence of porphyrin dimers inside the pores.

It is worth mentioning that chronoamperometry at longer times showed a slight decrease in current, although these preliminary results provide a sound basis for demonstrating that the formed dimer assists the photoelectrocatalytic performance of mesoporous titania thin films with stability for over 4 hours under operational conditions and similar photoelectrodes.[51,52] The structural integrity of the cMTTF is maintained with the properties and an organized pore network. However, the porphyrin dimer suffers desorption because of the high electrolyte concentration interfering in electrostatic interactions with the cMTTF pore surface.[16]

To summarize, while all three composites improve the photocurrent of cMTTF, the f-NiP/FeP system shows the greatest increase. The formation of metalloporphyrin μ-peroxo bridged dimers allows for an increased sensitizer loading inside the film pores. Furthermore, the bridging between metal centers and π–π overlapping might also play an important role in electron transfer. The presence of the dimer also seems to enhance oxygen evolution activity, since the axial coordination of oxygen species to the nickel metallic center allows the formation of intermediate oxygen species.

Conclusions

In this study, we have successfully synthesized and characterized cMTTF modified with FeP, NiP, and NiP/FeP, highlighting the importance of coordination chemistry in noncovalent bimetallic assemblies of porphyrins for photoelectrochemical applications. We have validated the cooperative effect of both metal complexes within this novel system, where the μ-peroxo-bridged interaction between Fe and Ni is integrated into a supramolecular heterometallic structure of porphyrins. The

inclusion of FeP and NiP together in the nanocomposite seems to form a bimetallic dimer, as seen from the shifts in Raman frequencies and XPS results. Furthermore, impedance analysis of the nanocomposites revealed reduced charge transfer resistance, providing clear evidence of the coordinated interaction between the metallic centres. Bimetallic surfaces displayed an enhanced catalytic activity compared to their monometallic counterparts, owing to the synergistic interplay between the iron and nickel centres. These interactions play a pivotal role in facilitating the electrocatalytic process. Additionally, our study demonstrates the potential of using mesoporous titania as a photoactive matrix for the rational design of highly efficient porphyrin-based photo electrocatalysts, with promising applications in various catalytic processes and mechanistic investigations. Overall, the functionalization of crystalline mesoporous titania thin films with heterobimetallic systems sets the basis for new materials with enhanced photocatalytic and photosensitized activity.

Author contributions

Conceptualization: F. H. (lead), M. H.; methodology: F. H., R. C., P. V., M. H.; investigation: F. H., P. V.; formal analysis: F. H., P. V., R. C., M. H.; writing-original draft preparation: F. H., P. V., R. C., M. H.; writing-review and editing: F. H., P. V., R. C., G. J. A. A. S. I., M. H.; supervision: G. J. A. A. S. I., M. H.; funding acquisition: G. J. A. A. S. I., M. H. (lead).

Conflicts of interest

There are no conflicts to declare.

Acknowledgements

References

1 E. Brillas, A. Serrà and S. Garcia-Segura, *Curr. Opin. Electrochem.*, 2021, **26**, 100660.

2 B. Morgan and D. Dolphin, in *Metal Complexes with Tetrapyrrole Ligands I*, Springer-Verlag, Berlin/Heidelberg, 2005, pp. 115–203.

3 L. K. Blusch, *The Siamese-Twin Porphyrin and its Copper and Nickel Complexes: A Non-innocent Twist*, Springer International Publishing, Cham, 2013.

4 M. Hamer, R. R. Carballo and I. N. Rezzano, *Electroanalysis*, 2009, **21**, 2133–2138.

5 M. Hamer, R. R. Carballo and I. N. Rezzano, *Sens. Actuators, B*, 2011, **160**, 1282–1287.

6 M. Hamer, R. R. Carballo, N. Cid and I. N. Rezzano, *Electrochim. Acta*, 2012, **78**, 302–307.

7 M. Hamer and I. N. I. N. Rezzano, *Inorg. Chem.*, 2016, **55**, 8595–8602.

8 Q. Li, Y. Bao and F. Bai, *MRS Bull.*, 2020, **45**, 569–573.

9 M. Vartanian, R. Singhal, P. de la Cruz, G. D. Sharma and F. Langa, *Chem. Commun.*, 2018, **54**, 14144–14147.

10 J. Meng, Z. Xu, H. Li, D. James Young, C. Hu and Y. Yang, *ChemCatChem*, 2021, **13**, 1396–1402.

11 X. Fang, L. Jiao, R. Zhang and H.-L. Jiang, *ACS Appl. Mater. Interfaces*, 2017, **9**, 23852–23858.

12 J. Sun, H. Yin, P. Liu, Y. Wang, X. Yao, Z. Tang and H. Zhao, *Chem. Sci.*, 2016, **7**, 5640–5646.

13 C. Wu, X. Zhang, Z. Xia, M. Shu, H. Li, X. Xu, R. Si, A. I. Rykov, J. Wang, S. Yu, S. Wang and G. Sun, *J. Mater. Chem. A*, 2019, **7**, 14001–14010.

14 P. Vensaus, Y. Liang, F. C. Herrera, G. J. A. A. Soler-Illia and M. Lingenfelder, *Int. J. Hydrogen Energy*, 2024, **59**, 89–96.

15 P. Vensaus, R. M. Caraballo, E. Tritto, C. C. Fernández, P. C. Angelomé, M. C. Fuertes, F. J. Williams, G. J. A. A. Soler-Illia and L. M. Baraldo, *Eur. J. Inorg. Chem.*, 2023, **27**, e202300576.

16 R. M. Caraballo, P. Vensaus, F. C. Herrera, G. J. A. A. Soler Illia and M. Hamer, *RSC Adv.*, 2021, **11**, 31124–31130.

17 F. C. Herrera, V. Sireus, P. Rassu, L. Stagi, M. Reale, A. Sciortino, F. Messina, G. J. A. A. Soler-Illia, L. Malfatti and P. Innocenzi, *Chem. Mater.*, 2023, **35**, 8009–8019.

18 G. J. A. A. Soler-Illia, P. Vensaus and D. Onna, in *Chemical Solution Synthesis for Materials Design and Thin Film Device Applications*, Elsevier, 2021, pp. 195–229.

19 I. L. Violi, M. D. Perez, M. C. Fuertes and G. J. A. A. Soler-Illia, *ACS Appl. Mater. Interfaces*, 2012, **4**, 4320–4330.

20 R. M. Caraballo, D. Onna, N. López Abdala, G. J. A. A. Soler Illia and M. Hamer, *Sens. Actuators, B*, 2020, **309**, 127712.

21 M. Hamer, R. M. Caraballo, P. J. Eaton and C. Medforth, *J. Porphyrins Phthalocyanines*, 2019, **23**, 526–533.

22 A. Calvo, M. C. Fuertes, B. Yameen, F. J. Williams, O. Azzaroni and G. J. A. A. Soler-Illia, *Langmuir*, 2010, **26**, 5559–5567.

23 M. Yu, G. Moon, E. Bill and H. Tüysüz, *ACS Appl. Energy Mater.*, 2019, **2**, 1199–1209.

24 M. Hamer, J. P. Tomba and I. N. Rezzano, *Sens. Actuators, B*, 2014, **193**, 121–127.

25 S. Rywkin, C. M. Hosten, J. R. Lombardi and R. L. Birke, *Langmuir*, 2002, **18**, 5869–5880.

26 R. Holze, *Electrochim. Acta*, 1988, **33**, 1619–1627.

27 L. M. C. Ferreira, D. Grasseschi, M. S. F. Santos, P. R. Martins, I. G. R. Gutz, A. M. C. Ferreira, K. Araki, H. E. Toma and L. Angnes, *Langmuir*, 2015, **31**, 4351–4360.

28 E. Martínez-Periñán, M. Revenga-Parra, J. Pastore, F. Pariente, F. Zamora, O. Castillo, E. Lorenzo and H. D. Abruña, *J. Phys. Chem. C*, 2018, **122**, 12377–12383.

29 K. Kalyanasundaram and M. Neumann-Spallart, *J. Phys. Chem.*, 1982, **86**, 5163–5169.

30 K. T. Yue, M. Lin, T. A. Gray and L. G. Marzilli, *Inorg. Chem.*, 1991, **30**, 3214–3222.

31 M. Adinehnia, J. R. Eskelsen, K. W. Hipps and U. Mazur, *J. Porphyrins Phthalocyanines*, 2019, **23**, 154–165.

32 M. Adinehnia, B. Borders, M. Ruf, B. Chilukuri, K. W. Hipps and U. Mazur, *J. Mater. Chem. C*, 2016, **4**, 10223–10239.

33 C. W. Leishman and J. L. McHale, *J. Phys. Chem. C*, 2015, **119**, 28167–28181.

34 A. J. Olaya, D. Schaming, P.-F. Brevet, H. Nagatani, T. Zimmermann, J. Vanicek, H.-J. Xu, C. P. Gros, J.-M. Barbe and H. H. Girault, *J. Am. Chem. Soc.*, 2012, **134**, 498–506.

35 M. Lanznaster, A. Neves, A. J. Bortoluzzi, V. V. E. Aires, B. Szpoganicz, H. Terenzi, P. C. Severino, J. M. Fuller, S. C. Drew, L. R. Gahan, G. R. Hanson, M. J. Riley and G. Schenk, *JBIC, J. Biol. Inorg. Chem.*, 2005, **10**, 319–332.

36 S. Dutta and P. Biswas, *Polyhedron*, 2012, **31**, 110–117.

37 A. Neves, M. Lanznaster, A. J. Bortoluzzi, R. A. Peralta, A. Casellato, E. E. Castellano, P. Herrald, M. J. Riley and G. Schenk, *J. Am. Chem. Soc.*, 2007, **129**, 7486–7487.

38 T. Marshall-Roth, N. J. Libretto, A. T. Wrobel, K. J. Anderton, M. L. Pegis, N. D. Ricke, T. Van Voorhis, J. T. Miller and Y. Surendranath, *Nat. Commun.*, 2020, **11**, 5283.

39 W. Orellana, C. Z. Loyola, J. F. Marco and F. Tasca, *Sci. Rep.*, 2022, **12**, 8072.

40 Y. Dou, A. Wang, L. Zhao, X. Yang, Q. Wang, M. Shire Sudi, W. Zhu and D. Shang, *J. Colloid Interface Sci.*, 2023, **650**, 943–950.

41 Q. Wang, J. Ren, A. Wang, Y. Dou, M. S. Sudi, W. Zhu and L. Li, *Dyes Pigm.*, 2022, **206**, 110683.

42 Y. Liu, K. Zhang, K. Wang, M. Wang, Y. Liu, J. Jiang, T. Liu, E. Liang and B. Li, *Appl. Catal., B*, 2022, **318**, 121890.

43 J. C. Yu, J. Yu and J. Zhao, *Appl. Catal., B*, 2002, **36**, 31–43.

44 W. He, Y. Zhu, G. Zeng, Y. Zhang, Y. Wang, M. Zhang, H. Long and W. Tang, *Chem. Eng. J.*, 2020, **392**, 123640.

45 J. Lv, L. Wang, R. Li, K. Zhang, D. Zhao, Y. Li, X. Li, X. Huang and G. Wang, *ACS Catal.*, 2021, **11**, 14338–14351.

46 T. Zhou, Z. Cao, H. Wang, Z. Gao, L. Li, H. Ma and Y. Zhao, *RSC Adv.*, 2017, **7**, 22818–22824.

47 J. Nai, Y. Tian, X. Guan and L. Guo, *J. Am. Chem. Soc.*, 2013, **135**, 16082–16091.

48 N. Li, D. K. Bediako, R. G. Hadt, D. Hayes, T. J. Kempa, F. von Cube, D. C. Bell, L. X. Chen and D. G. Nocera, *Proc. Natl. Acad. Sci. U. S. A.*, 2017, **114**, 1486–1491.

49 J. Chen, F. Zheng, S.-J. Zhang, A. Fisher, Y. Zhou, Z. Wang, Y. Li, B.-B. Xu, J.-T. Li and S.-G. Sun, *ACS Catal.*, 2018, **8**, 11342–11351.

50 W. Wan, Y. Zhao, S. Wei, C. A. Triana, J. Li, A. Arcifa, C. S. Allen, R. Cao and G. R. Patzke, *Nat. Commun.*, 2021, **12**, 5589.

51 P. Vensaus, L. N. Mendioroz, F. C. Herrera, M. P. Kreuzer, F. A. Viva and G. J. A. A. Soler Illia, *ACS Appl. Eng. Mater.*, 2024, **2**, 224–235.

52 E. Gent, D. H. Taffa and M. Wark, *Coatings*, 2019, **9**, 625.

53 A. Wolcott, W. A. Smith, T. R. Kuykendall, Y. Zhao and J. Z. Zhang, *Small*, 2009, **5**, 104–111.

54 I. S. Cho, M. Logar, C. H. Lee, L. Cai, F. B. Prinz and X. Zheng, *Nano Lett.*, 2014, **14**, 24–31.

55 D. Qiu, C. He, Y. Lu, Q. Li, Y. Chen and X. Cui, *Dalton Trans.*, 2021, **50**, 15422–15432.

56 L. M. C. Ferreira, P. R. Martins, K. Araki and L. Angnes, *Electroanalysis*, 2019, **31**, 688–694.